JOURNAL OF PROPULSION AND POWER
Vol. 13, No. 5, September–October 1997

# Applications of Algebraic Reynolds Stress Turbulence Models Part 2: Transonic Shock-Separated Afterbody

John R. Carlson*
*NASA Langley Research Center, Hampton, Virginia 23681*

**The ability of the three-dimensional Navier–Stokes method PAB3D code to simulate the effect of Reynolds number variation using nonlinear explicit algebraic Reynolds stress turbulence modeling was assessed. Surface pressure coefficient distributions and integrated drag predictions on an axisymmetric nozzle afterbody were compared with experimental data at Reynolds numbers from 10 to 130 × $10^6$. There was generally good agreement of surface static pressure coefficients between the computational fluid dynamics (CFD) and measurement. The change in pressure coefficient distributions with varying Reynolds number was similar to the experimental data trends, though the CFD slightly overpredicted the effect. The computational sensitivity of viscous modeling and turbulence modeling are shown. Integrated afterbody pressure drag was typically slightly lower than the experimental data. The change in afterbody pressure drag with Reynolds number was small, both experimentally and computationally, even though the shape of the distribution was somewhat modified with the Reynolds number.**

## Nomenclature

$A_{\max}$ = maximum body cross-sectional area, 0.78539 in.$^2$
$C_D$ = pressure drag coefficient, $F/q_\infty A_{\max}$
$C_p$ = pressure coefficient, $p - p_\infty/q_\infty$
$d_m$ = body maximum diameter, 1.0 in.
$F$ = axial force along body axis
$h_1$ = physical height of first computational grid from a wall
$K$ = turbulent kinetic energy
$L$ = model reference length
$M$ = Mach number
$p$ = static pressure, Pa
$q$ = dynamic pressure, Pa
$R$ = Reynolds number based on model reference length
$T$ = temperature
$t$ = time
$x$ = streamwise distance
$z$ = vertical distance
$\varepsilon$ = turbulent dissipation
$\phi$ = angular location of pressure orifices, deg

*Subscripts*
fp = flat plate
ref = reference body cross-sectional area
$t_0$ = freestream total condition
sf = skin friction contribution
$\beta$ = nozzle–boat-tail component contribution
$\infty$ = freestream condition

## Introduction

RECENTLY, many aircraft program efforts consider the difficulty of Reynolds number scaling a significant aspect of aircraft testing and development. Wing aerodynamics and flow about propulsion systems can have considerable sensitivity to varying Reynolds numbers. Most subscale wind-tunnel tests occur at Reynolds numbers below those of flight conditions; therefore, the ability of computational fluid dynamics (CFD) to simulate higher Reynolds number flow is important.

Prior to the development of cryogenic test techniques for achieving high Reynolds numbers in wind-tunnel facilities, little fundamental research data had been available for the evaluation of any theoretical methods to predict these effects. Several years ago, during the development phase of cryogenic testing techniques at the NASA Langley Research Center, two sets of simple axisymmetric nacelle models were built and tested in what was then known as the 1/3-m Pilot Transonic Cryogenic Tunnel (now the NASA Langley 0.3-Meter Transonic Cryogenic Tunnel). This tunnel produced some of the first sets of subscale nozzle–boat-tail geometry test data obtained over a large range of Reynolds numbers.[1–4] Another report evaluated the fundamental capability of predicting flat-plate flow at very high Reynolds numbers.[5] This report assesses the capability of the Navier–Stokes method PAB3D code,[6–9] using nonlinear algebraic Reynolds stress turbulence models to predict the Reynolds number effects on the flow about a nozzle boat-tail with flow separation. Comparisons were made with wind-tunnel data at $M = 0.9$ over a wide range of Reynolds numbers.

## Computational Procedure

The code PAB3D is a general three-dimensional Navier–Stokes method. Version 13S was used in this investigation. This code has several computational schemes and different turbulence and viscous stress models that can be utilized.[6–8] The governing equations are the Reynolds-averaged simplified Navier–Stokes (RANS) equations obtained by neglecting all streamwise derivatives of the viscous terms. The resulting equations are written in generalized coordinates and conservative form. Viscous model options include thin-layer assumptions in *j* and *k* directions or fully coupled *j*-*k*. Typically, the full three-dimensional viscous stresses are reduced to a thin-layer assumption, and all but one direction are eliminated completely, but this assumption must be made with caution. Experiments such as supersonic flow through a square duct require fully coupled two-directional viscosity to properly predict the physics of the secondary crossflow. The Roe upwind scheme with first-, second-, or third-order accuracy can be

---

Presented as Paper 96-2544 at the AIAA/ASME/SAE/ASEE 32nd Joint Propulsion Conference, Lake Buena Vista, FL, July 1–3, 1996; received Aug. 20, 1996; revision received May 7, 1997; accepted for publication May 7, 1997.

*Senior Scientist, Aero- and Gasdynamics Division, M/S 286.

used in evaluating the explicit part of the governing equations, and the van Leer scheme is used to construct the implicit operator. The diffusion terms are centrally differenced and the inviscid-flux terms are upwind differenced. Two finite volume flux-splitting schemes are used to construct the convective-flux terms.

The code has options to calculate flow using several explicit algebraic Reynolds stress turbulence models. The models of Shih, Zhu, and Lumley (SZL), Gatski and Speziale (GS), and Girimaji (G) are detailed in a companion paper.[5]

## Results and Discussion

### Test Facility

The test case was an axisymmetric geometry that was part of a series of models tested in both the NASA Langley 0.3-m Pilot Transonic Cryogenic Tunnel and the NASA Langley 16-Foot Transonic Tunnel. The pilot tunnel had an octagonal test section with slots at the corners of the octagon and was essentially a scale model of the NASA Langley 16-Foot Transonic Tunnel test section.[10] The test medium for the cryogenic tunnel was air that was cooled by liquid nitrogen. High Reynolds number data were obtained in the pilot tunnel through a combination of cryogenic freestream temperatures and freestream total pressures that were independently controllable. Approximately 5 atm of pressure and 100 K total temperature produced a unit Reynolds number of 260 × $10^6$/m.

The experiment was conducted over a range of temperatures from approximately 100 to 300 K and pressures from 1 to 5 times the standard atmospheric level. Several settings of freestream total temperatures or pressures can result in identically set Reynolds numbers. Surface pressure coefficients and nozzle–boat-tail drag were shown to be similar regardless of the temperature and pressure combinations that created the equivalent Reynolds numbers.[2] High Reynolds number simulations with the CFD method were obtained through increased total pressure rather than through a combination of freestream total pressure and cryogenic temperatures. The temperature range of Sutherland's law used for calculating bulk viscosity imposes some limits to the input flow conditions. Though data were obtained over a range of Mach numbers from 0.6 to 0.9, only the $M = 0.9$ data are compared with the CFD in this paper. Table 1 is a list of the tunnel conditions for the experimental data obtained at $M = 0.9$ for the $L/d_m = 16.0$ model.

### Axisymmetric Afterbody Model and Conditions

The configuration used for this study was one of six models that were built for the original Reynolds number study.[1] Four models with different boat-tail geometry were associated with a body length of 8 in. from the nose to the start of the boat-tail (characteristic length) and two models with a characteristic length of 16 in. The boat-tail geometries had circular–arc, circular–arc–conic, or contoured profiles. This investigation utilized the circular arc with a length-to-maximum-diameter ratio (fineness ratio) of 0.8 boat-tail. Figure 1 is a photograph of the model mounted in the pilot tunnel. The nose of the model was a 28-deg cone, 1.7956-in.-long, fairing to the cylindrical body via a 1.3615-in.-radius circular arc whose center is 2.125 in. downstream of the model nose and 0.8615 in. below the model centerline. The circular-arc fairing is tangent at its endpoints to the conical nose (1.7956 in. from the nose) and cylindrical body (2.125 in. from the nose). The model was sting mounted with the diameter of the sting being equal to the model base diameter. The length of the constant diameter portion of the sting (6.70 in. measured from the nozzle connect station) was such that, based on the work of Cahn,[11] there should be no effect of the sting flare downstream of the nozzle trailing edge on the boat-tail pressure distributions. These numbers will produce an analytically consistent surface definition. The model was cast aluminum and not manufactured to these tolerances.

Table 1 Range of conditions for the experimental data

| $M_\infty$ | $T_{t_0}$, K (R) | $p_{t_0}$, atm | $R$ (×$10^6$) |
|---|---|---|---|
| 0.903 | 106 (191) | 4.98 | 128 |
| 0.908 | 118 (212) | 3.98 | 87 |
| 0.901 | 119 (214) | 2.98 | 64 |
| 0.911 | 118 (212) | 2.47 | 55 |
| 0.910 | 118 (212) | 1.97 | 43 |
| 0.904 | 119 (214) | 1.49 | 32 |
| 0.903 | 118 (212) | 1.24 | 27 |
| 0.899 | 312 (562) | 4.97 | 28 |
| 0.899 | 308 (554) | 3.79 | 22 |
| 0.902 | 308 (554) | 2.48 | 14 |
| 0.901 | 307 (553) | 1.23 | 7 |

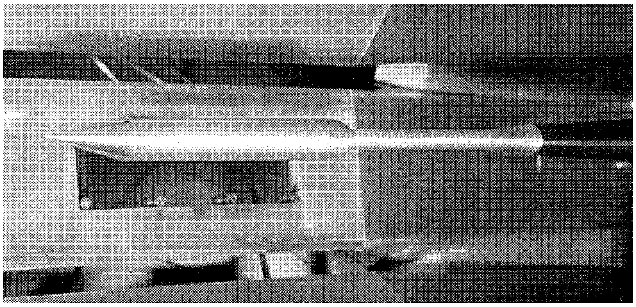

**Fig. 1 Eight-in. axisymmetric afterbody model in the 0.3-m NASA Langley Pilot Transonic Cryogenic Tunnel.**

The axisymmetric afterbody grid utilized H–O type mesh topology with all block dimensions divisible by 4. The mesh was gridded with a single-cell 5-deg-wide wedge grid with the streamwise flow direction oriented along the $j$ index to utilize the implicit flow solver in the code for faster solution convergence. The body was described using 100 cells extending from the leading edge of the nose to the nozzle connect station. There were 80 cells extending from the nozzle connect station to the nozzle–boat-tail trailing edge. There were 80 cells extending 80 body radii from the body surface to the far field. There was approximately a 16% expansion rate in the boundary-layer grid. The inflow boundary was 40 body radii upstream of the model nose, and the outflow boundary was 35 radii downstream of the nozzle boat-tail. Solid walls were treated as no-slip adiabatic surfaces. A boundary condition for the Riemann invariants along the characteristics was specified for the freestream inflow face and the lateral freestream outer boundary of the flow domain. An extrapolation boundary condition was applied on the downstream outflow face. The freestream conditions for axisymmetric CFD cases were $M = 0.9$ and $T_{t_0} = 540R$, using air at $\gamma = 1.4$. The first cell height of the grid of each configuration was different for each freestream Reynolds number according to Table 2.

The wind-tunnel models were constructed of cast aluminum with stainless-steel pressure tubes cast as an integral part of the model. The model was instrumented with 30 pressure orifices in three rows of 10 orifices each. The 1-in. diameter of the model physically precluded the placement of all 30 orifices along the same row. Table 3 is a tabulation of the orifice locations.

### Grid Convergence

Figures 2 and 3 show grid sensitivity of the Girimaji algebraic Reynolds stress model (ASM) at $M = 0.9$ at the lowest and highest Reynolds number for this test case, $R = 7$ and 128 × $10^6$, respectively. These sensitivities were relatively consistent for the other turbulence and viscous models investigated. A few exceptions occurred where the coarse-grid solution did not converge, but the following medium- and fine-grid solu-

Table 2 Schedule of pressure and grid height with Reynolds number

| R ($\times 10^6$) | $p_{t_0}$, atm (psi) | $h_1$ (in.) |
|---|---|---|
| 7.0 | 1.21 (17.8) | $6 \times 10^{-5}$ |
| 55.2 | 9.52 (140.) | $8 \times 10^{-6}$ |
| 128.3 | 22.1 (325.) | $2 \times 10^{-6}$ |

Table 3 Pressure orifice locations on wind-tunnel model

| $x/d_m$ for $L/d_m = 16$ | | |
|---|---|---|
| $\phi$ = 0 deg | $\phi$ = 120 deg | $\phi$ = 240 deg |
| −0.4491 | −0.4660 | −0.4561 |
| −0.1637 | −0.2201 | −0.1552 |
| −0.0600 | −0.1281 | −0.0590 |
| 0.0337 | −0.0260 | 0.0390 |
| 0.1268 | 0.0744 | 0.1342 |
| 0.2279 | 0.1729 | 0.2713 |
| 0.3210 | 0.2696 | 0.3718 |
| 0.4199 | 0.3679 | 0.4680 |
| 0.5231 | 0.4640 | 0.5749 |
| 0.6279 | 0.6758 | 0.7304 |

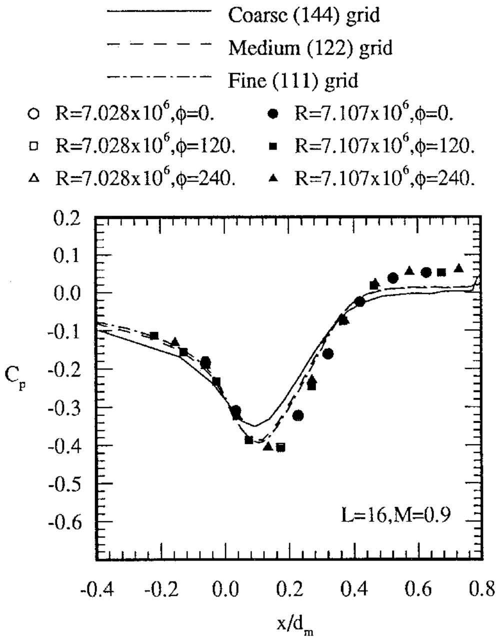

Fig. 2 Grid sensitivity at $R = 7 \times 10^6$, Girimaji ASM, min-mod limiter, $k$ thin layer.

tions converged and the results were similar in nature to those shown in Figs. 2 and 3. In a few instances, the coarsest grid density is too sparse and generates errors in the solution that prevent convergence. All solutions were fairly well-grid converged and solution converged. Initially, in Fig. 3, the coarse grid solution appears to be the best match with the data; however, further refinement of the grid revealed this solution to not be grid converged. Solutions for this geometry appear to require between 40–80 cells along the nozzle boat-tail to predict the shock-separated flow reasonably accurately.

### Low Reynolds Number Computations

Figures 4–8 are low-Reynolds-number calculations showing the effect of turbulence model, turbulent trip location, and viscous model on pressure coefficient and turbulent kinetic energy distributions.

Aft-body surface pressure coefficients predicted by different turbulence models are shown in Fig. 4. All of these solutions used the $k$ thin-layer viscous model, min-mod limiter, and turbulent trip point 1, which was approximately 0.031 in. (0.08 cm) downstream of the nose. The three ASMs predicted a shock strength slightly weaker than the data and a pressure recovery slightly lower than the data. The standard $K$-$\varepsilon$ model, in this instance, appears to have better agreement with the data closely matching peak negative pressure and recovered to a static pressure only slightly above that of the data at the boat-tail trailing edge. Figure 5 is a plot of the peak turbulent kinetic energy for each turbulence model using the same parameters as the calculations in Fig. 4. For clarity, two areas of the axisymmetric body are detailed, the region downstream of the nose where the turbulent trip occurs and the region around the nozzle boat-tail. The large spike in $K/a^2$ just downstream of $x/d_m = -16$ is the turbulent trip impulse in $k$. None of the four turbulent models tested developed turbulent flow immediately

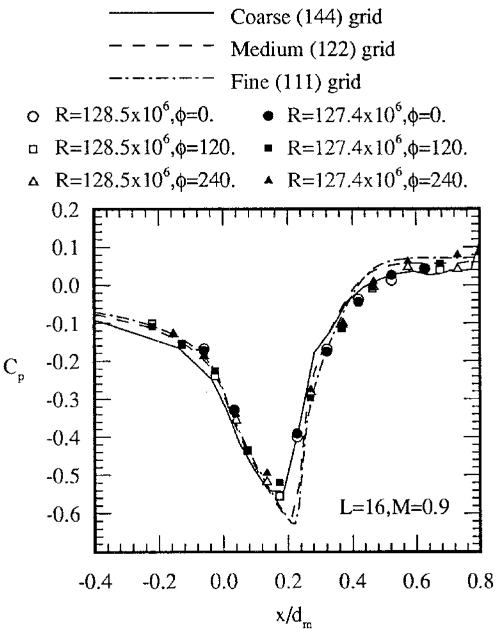

Fig. 3 Grid sensitivity at $R = 128 \times 10^6$, Girimaji ASM, min-mod limiter, $k$ thin layer.

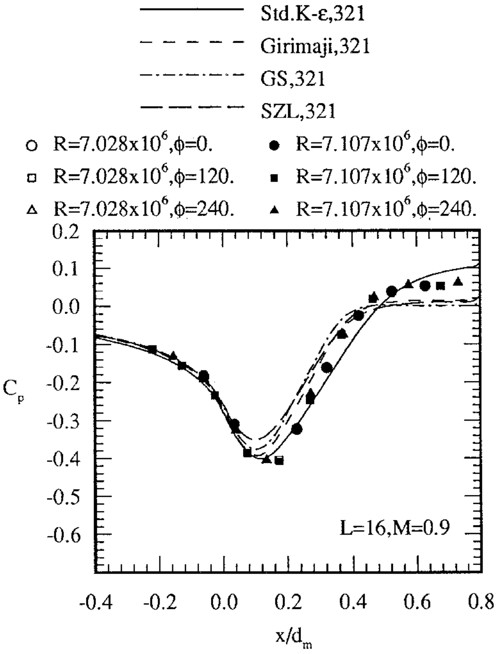

Fig. 4 Comparison of turbulence models with experimental data, $M = 0.9$, $R = 7 \times 10^6$.

downstream of the trip. The standard $K$-$\varepsilon$ linear model developed turbulence first, as indicated by the rise in $K/a^2$ around $x/d_m = -15.7$. The flow predicted by G and SZL ASMs became turbulent around $x/d_m = -15.3$, and GS became turbulent the furthest downstream at $x/d_m = -14.4$.

Early studies by the author simulating the incompressible flat-plate flow displayed similar characteristics. If the turbulent trip was placed upstream of the critical flow point, turbulence would not develop immediately downstream of the trip. Conversely, turbulence would develop immediately when the turbulent trip was placed downstream of the critical flow point. Considering this, a different turbulent trip point was chosen roughly between the furthest upstream and downstream turbulent development points noted previously, and solutions were redeveloped for the three ASMs. Figures 6–8 show that downstream of the cone–cylinder transition of body shape at approximately $x/d_m = -13$, despite the different initial development of turbulence (trip 1 was upstream trip at $x/d_m = -15.969$ and trip 2 was downstream trip at $x/d_m = -15.000$), no significant changes occur in the peak turbulent kinetic energy. Figure 9 is representative of the lack of influence of static pressure coefficient distribution on the nozzle boat-tail between the two turbulent trip points as determined by the min–mod solution limiter. Further parametric studies are needed to determine the boundary-layer behavior from other solution limiters with changes in the laminar-to-turbulent flow regions.

Figure 10 is a study of the effect of different viscous models on the flow on the afterbody. Three calculations were performed using $k$ thin-layer (321), $j$-$k$ viscosity coupled (322), and $j$-$k$ viscosity uncoupled (323) viscosity models with G ASM at $7 \times 10^6$ Reynolds number. The use of $j$-$k$ viscosity appears to improve the comparison with experimental data by creating a shock slightly stronger and further downstream than the $k$ thin-layer calculation, in addition to slightly raising the pressure recovery in the region of separated flow. As will be

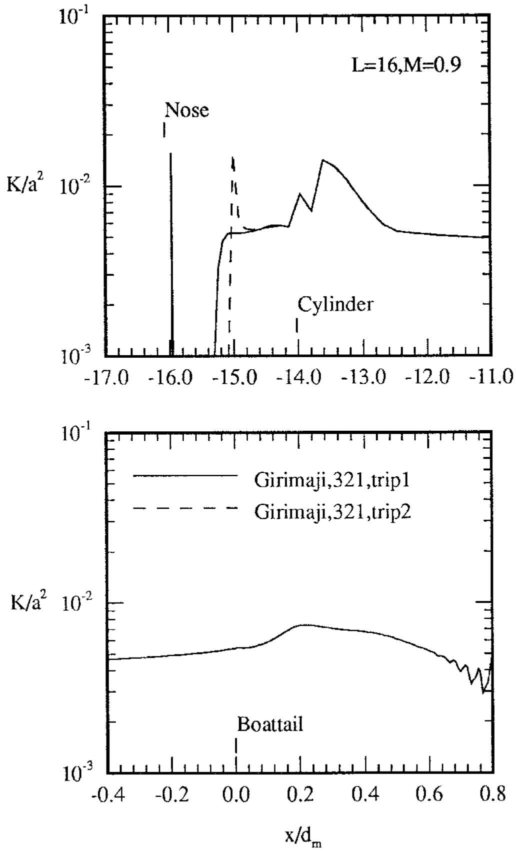

**Fig. 6 Effect of trip location on peak turbulent kinetic energy, $R = 7 \times 10^6$, min–mod, $k$ thin layer.**

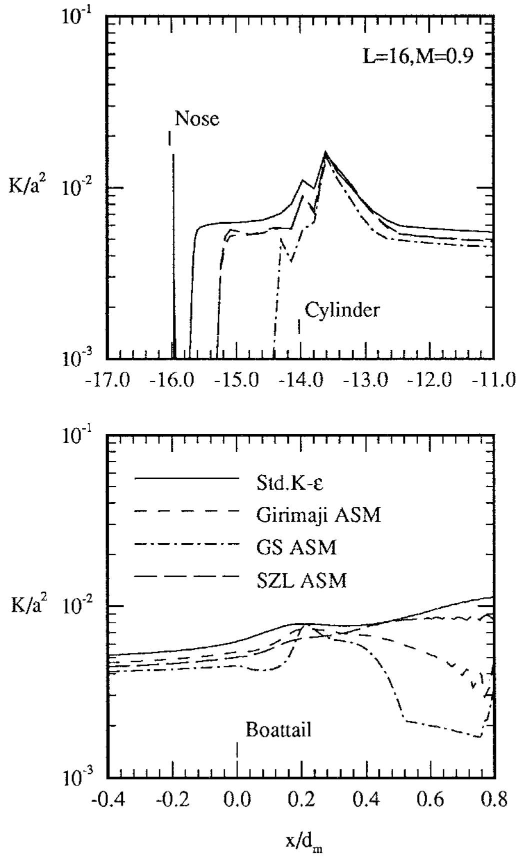

**Fig. 5 Peak turbulent kinetic energy in boundary layer, $R = 7 \times 10^6$, min–mod, $k$ thin layer.**

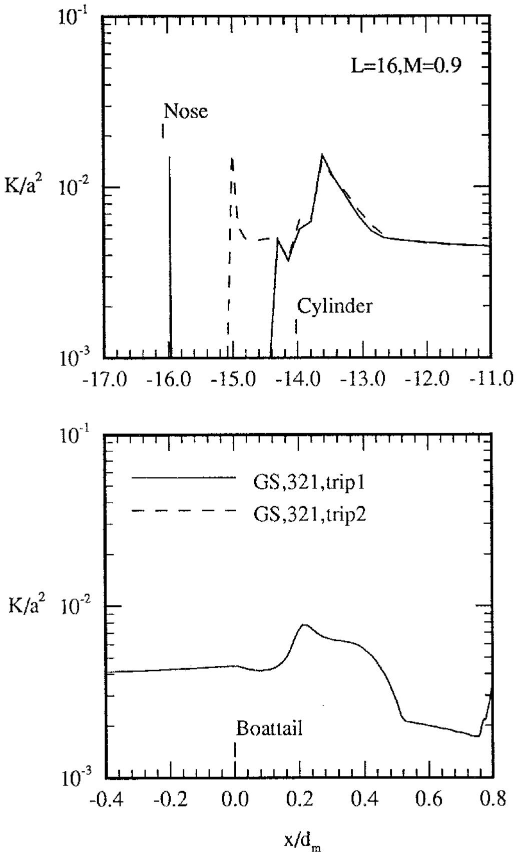

**Fig. 7 Effect of trip location on peak turbulent kinetic energy, $R = 7 \times 10^6$, min–mod, $k$ thin layer.**

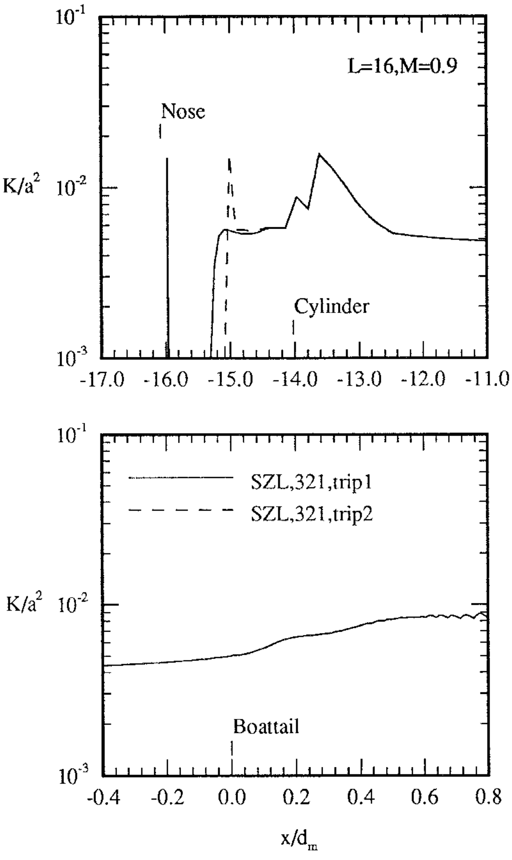

**Fig. 8 Effect of trip location on peak turbulent kinetic energy, $R = 7 \times 10^6$, min-mod, $k$ thin layer.**

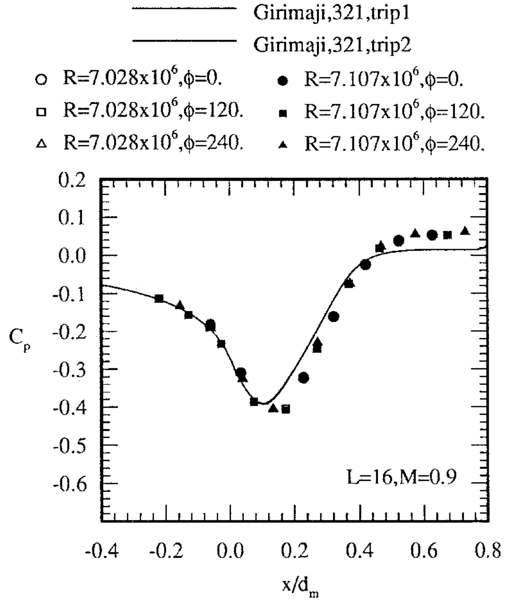

**Fig. 9 Effect of trip location on nozzle boattail pressure coefficients, $R = 7 \times 10^6$, $M = 0.9$.**

shown, the observations of best comparison with data changes with Reynolds number.

### High Reynolds Number Computations

Figures 11–15 are high Reynolds number calculations showing the effect of turbulence and viscous models on pressure coefficient and turbulent kinetic energy distributions on the body. Figure 11 is a comparison of the four turbulence models at $R = 128 \times 10^6$ using $k$ thin-layer viscosity, min-mod limiter, and trip 1 for turbulent tripping. The three ASMs cluster around the experimental data matching the pressure recovery in the separated flow region considerably better than at low Reynolds numbers. The standard $K$-$\varepsilon$ model predicts the strongest shock and highest pressure recovery.

Figure 12 is the plot of peak turbulent kinetic energy similar to Fig. 5 for the four turbulence models. Significantly, all four models developed turbulent flow immediately downstream of the turbulent trip as seen by the four curves departing from the trip spike in $K/a^2$ at levels around 0.004. Each turbulence model remained at slightly different levels, but had similar trends until the region of flow involving the shock separation downstream of $x/d_m = 0.25$. The trend of the peak turbulent kinetic energy was similar to the trend at a Reynolds number of $7 \times 10^6$ in Fig. 5. Though the three ASMs have very similar

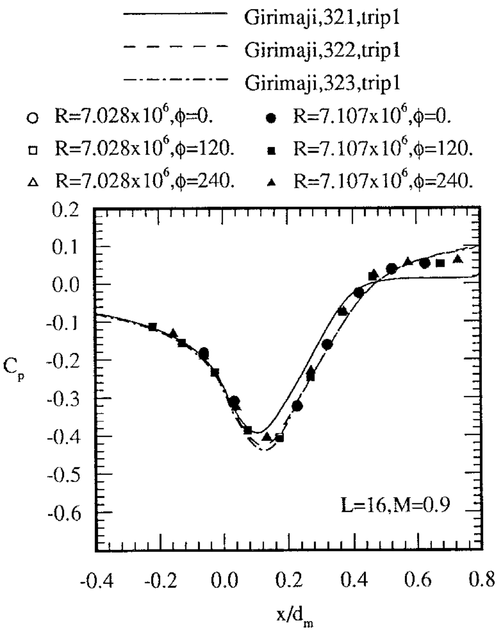

**Fig. 10 Effect of viscous model on nozzle boat-tail pressure coefficient distributions, $R = 7 \times 10^6$.**

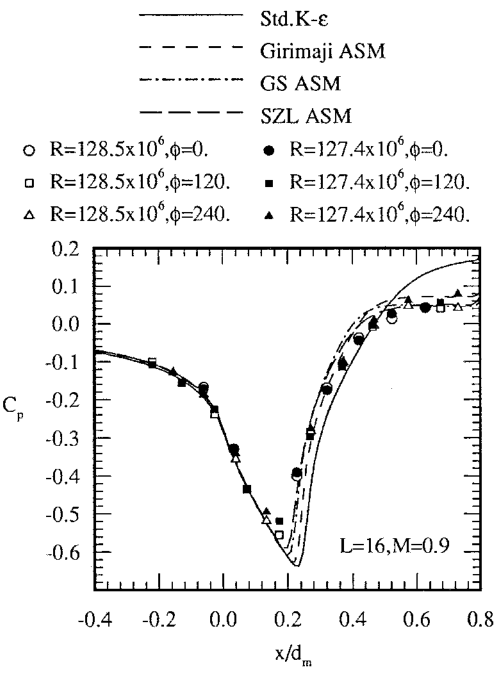

**Fig. 11 Comparison of turbulence models with experimental data, $R = 128 \times 10^6$, min-mod, $k$ thin layer, trip 1.**

static pressure coefficient distributions (Fig. 11), the peak $K/a^2$ trends are completely different. Also, the $C_p$ distributions between SZL and the standard $K$-$\varepsilon$ model are very different, but the peak $K/a^2$ have similar trends and levels. Therefore, at this point, a correlation between the trend of $K/a^2$ and $C_p$ cannot be made.

Figure 13 shows the effect of a viscous model that uses the Girimaji ASM at a Reynolds number of 128 × $10^6$. In this instance, the $k$ thin-layer calculation (321) provides the best comparison with the experimental pressure coefficient distribution. The $j$-$k$ viscous models behaved similarly in that the shock strength increased and the recovery pressure was higher than the $k$ thin-layer calculation. Figure 14 is the peak $K/a^2$ for the three viscous models shown in Fig. 13. The three viscous models have similar trends in peak turbulent kinetic energy until the region of shock-separated flow downstream of $x/d_m = 0.25$. Both $j$-$k$ viscous models generate higher peak turbulence than the $k$ thin-layer model. The plots in Fig. 15 are contours of turbulent kinetic energy predicted by the three viscous models previously discussed. The $k$ thin-layer viscous model, Fig. 15a, has an abrupt discontinuity in the flowfield around the boat-tail trailing edge, $x/d_m = 0.8$, whereas both $j$-$k$ viscous models predict very smooth and continuous contours from the region of the shock, $x/d_m = 0.25$, to downstream.

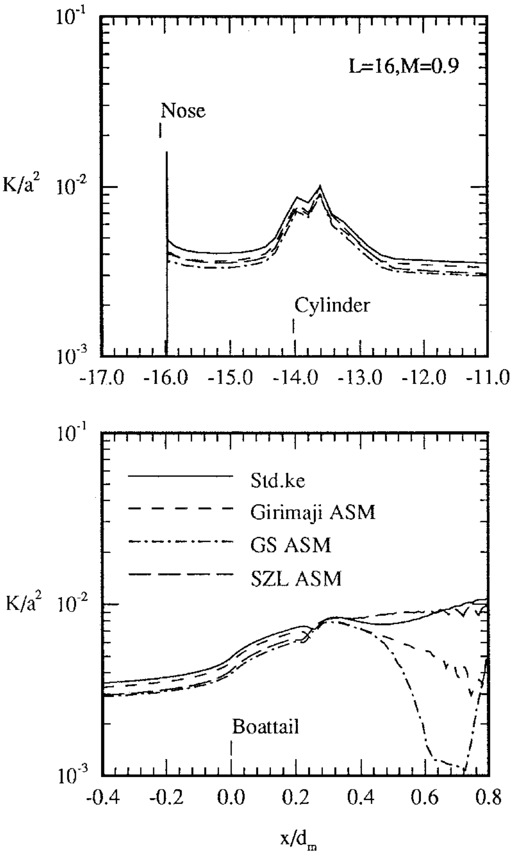

**Fig. 12 Peak turbulent kinetic energy in boundary layer, $R$ = 128 × $10^6$, min-mod, $k$ thin layer.**

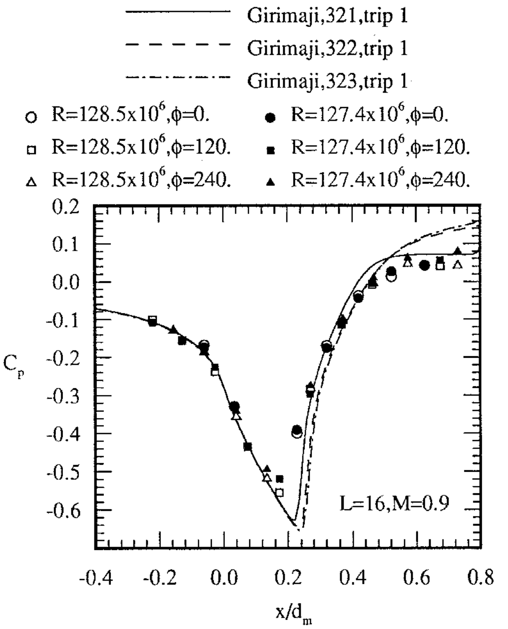

**Fig. 13 Effect of viscous model on nozle boat-tail pressure coefficient distributions, $R$ = 128 × $10^6$.**

### Reynolds Number Trends

Figures 16–21 are trends of integrated boat-tail pressure drag, skin friction, and predicted point of flow separation with Reynolds number. The integrated pressure drag variation with Reynolds number comparing CFD results with experiment is shown in Fig. 16. Despite the changes in the shock strength and pressures on the nozzle boat-tail with Reynolds number; the variation in pressure drag was small. Overall, the predicted level of pressure drag was slightly below that of the experimental data, though at the low and high Reynolds numbers the CFD calculation was almost within the scatter of the experimental data. As a point of reference, three additional data points are plotted to include data obtained for the short cryogenic models tested in the NASA Langley 16-Foot Transonic Tunnel, and the original 48-in. model also tested in this tunnel.

Figure 17 shows the predicted change in static pressure coefficient distribution with Reynolds number. The largest change seems to occur from the very low Reynolds number to

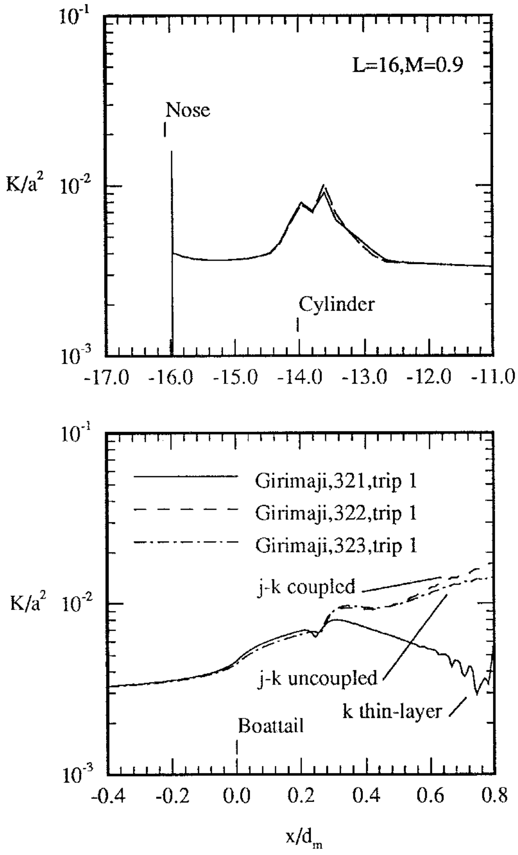

**Fig. 14 Peak turbulent kinetic energy in boundary layer, $R$ = 128 × $10^6$, min-mod, $k$ thin layer.**

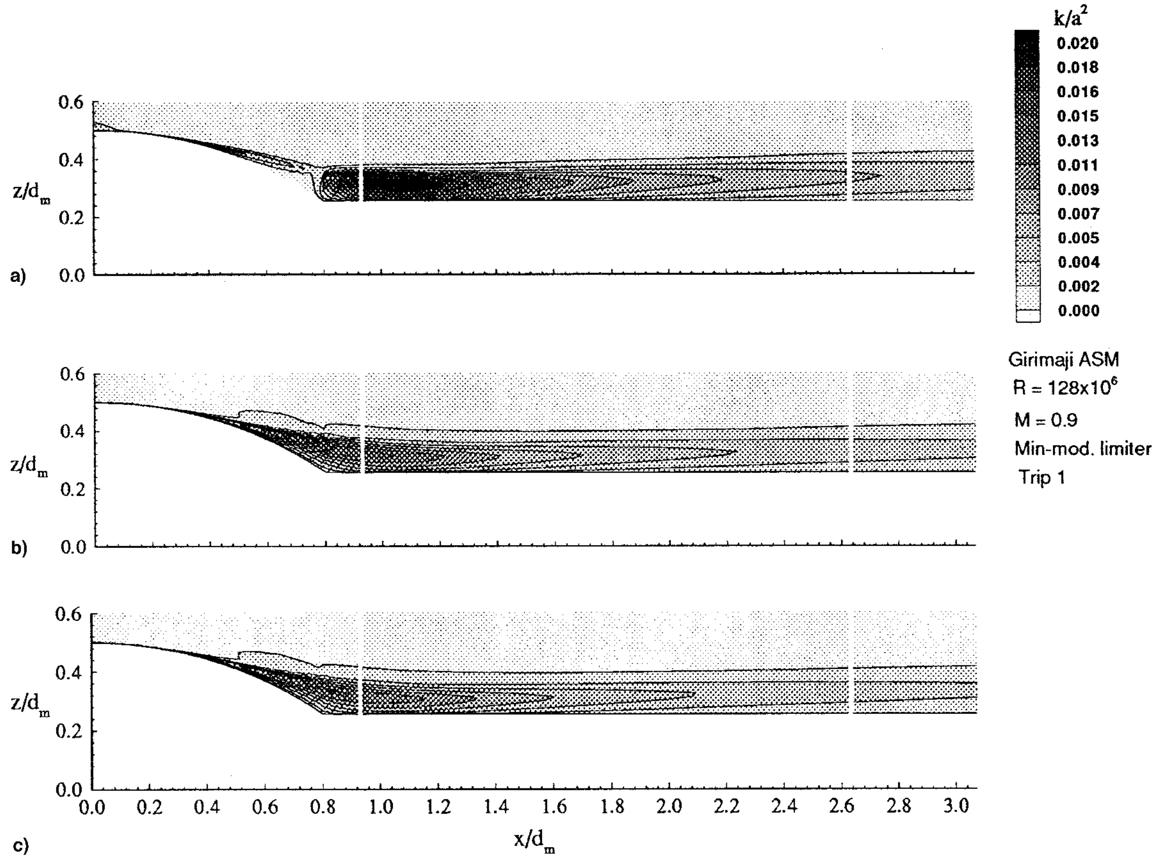

Fig. 15 Effect of viscous model on turbulent kinetic energy contours: a) *k* thin layer, b) *j*-*k* uncoupled, and c) *j*-*k* coupled.

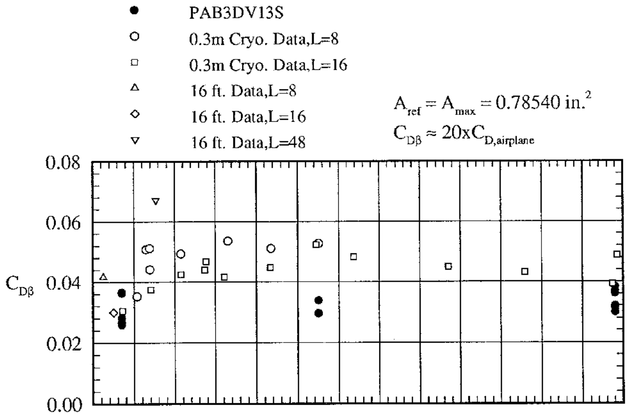

Fig. 16 Comparison of predicted integrated pressure boat-tail drag with experimental data, $M = 0.9$.

the midrange, with the code predicting a large increase in the peak velocity, a downstream shift of the peak, and a slight elevation of the static pressure of the flow in the region of separation. Considerably less change was predicted between the midrange and high Reynolds number of 128 × 10$^6$.

Figure 18 is a bar chart of the integrated pressure drag on the boat-tail at a Reynolds number of 7 × 10$^6$ that compares the different viscous models and trip location drag predicted from the Girimaji ASM with experimental data. The higher recovery pressure that occurred through the *j*-*k* viscosity calculations reduced the integrated pressure drag from 37 to roughly 28 nozzle drag counts. The scatter in the CFD results is about the same as the experimental results, with the exception of the 48-in. model data tested in the NASA Langley 16-Foot Transonic Tunnel.

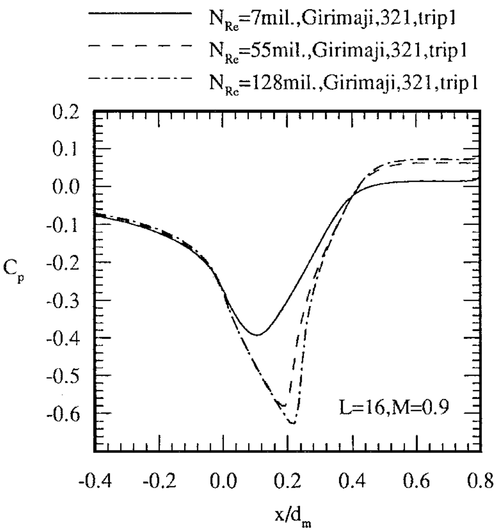

Fig. 17 Predicted variation of nozzle–boat-tail pressure coefficient distributions, $M = 0.9$.

High Reynolds number comparisons are shown in Fig. 19 with the addition of GS, SZL, and standard *K*-*ε*. The scatter in the CFD is similar to the low Reynolds number comparison with the standard *K*-*ε* that predicted the lowest drag caused by the considerably higher pressure recovery at the boat-tail. Girimaji and SZL *k* thin-layer data are the closest to the experimental data, though on average they are low.

Variation of predicted skin friction coefficients with Reynolds numbers for Girimaji ASM is plotted against flat-plate wetted area estimations in Fig. 20. In general, the CFD predicts skin friction coefficients are 3.5 nozzle drag counts low at a Reynolds number of 7 × 10$^6$ and about 1.5 nozzle drag counts

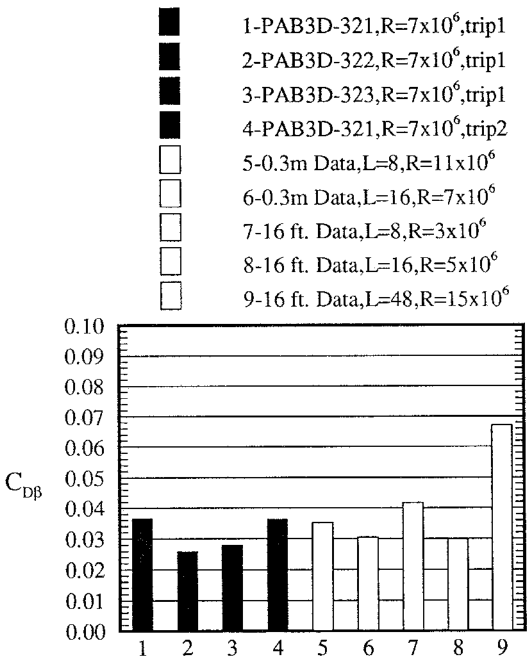

**Fig. 18 Comparison of integrated nozzle-boat-tail pressure drag at $R \approx 7 \times 10^6$, Girimaji ASM, $M = 0.9$.**

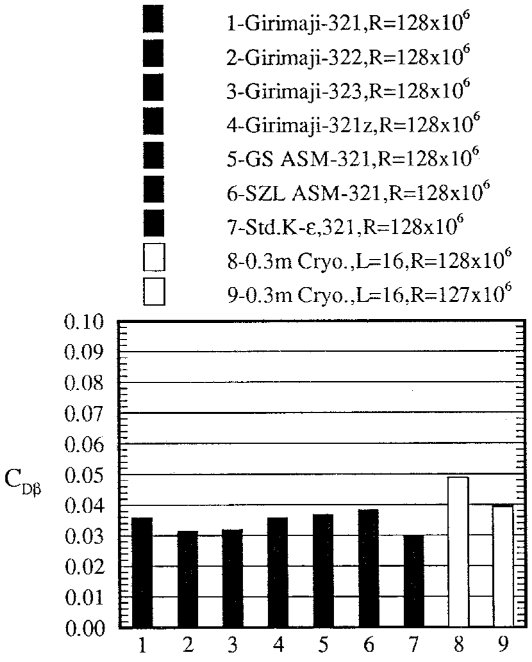

**Fig. 19 Comparison of integrated nozzle-boat-tail pressure drag at $R \approx 128 \times 10^6$, $M = 0.9$.**

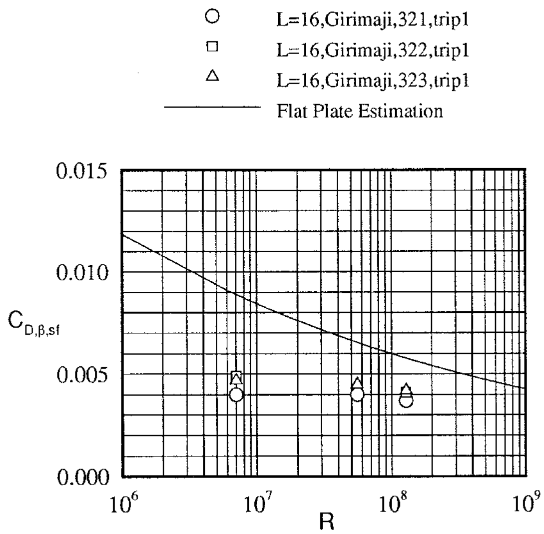

**Fig. 20 Comparison of predicted skin friction coefficients with wetted-area, flat-plate estimations, $M = 0.9$.**

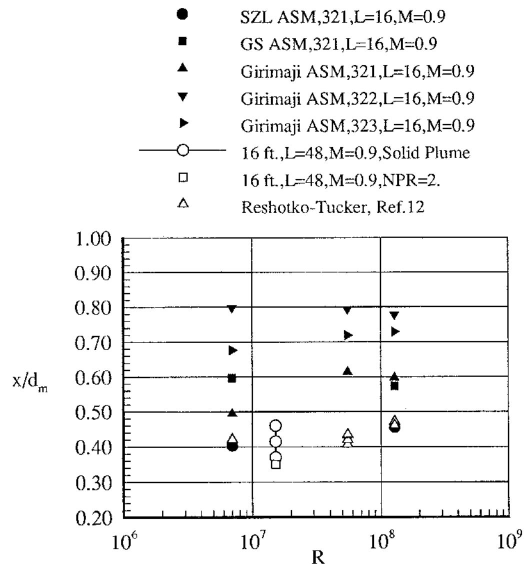

**Fig. 21 Variation of predicted point of flow separation compared with flow visualized data and a parametric theory.**

low at a Reynolds number of $128 \times 10^6$. Considering the flow effects not accounted for by the flat-plate wetted area calculations (e.g., nonconstant Mach number, adverse/favorable pressure gradients, aft-projected areas, and separated flow), this comparison is fairly good.

Figure 21 is an analysis of the predicted point of flow separation with a Reynolds number compared with some flow visualization data obtained in the NASA Langley 16-Foot Transonic Tunnel, with the 48-in. model in 1974 and the parametric theory of Reshotko-Tucker.[12] The separation observed in Ref. 18 was three dimensional, with the estimated extent shown by the spread in open triangles in Fig. 21. No separation data are available for this model at any of the other Reynolds numbers. The SZL ASM predicted a flow separation point that more closely matched the wind-tunnel measurement and Reshotko-Tucker predictions with increasing Reynolds numbers. Both Girimaji and GS predicted flow separation points further downstream. Girimaji's *j-k* viscosity observations predicted the least separated flows, with the *j-k* coupled viscosity calculation predicting practically no separated flow at a Reynolds number of $7 \times 10^6$.

## Summary

Linear turbulence simulations predict a shock further downstream and a recovery pressure higher than the nonlinear turbulence simulations at low and high Reynolds numbers for an axisymmetric afterbody geometry at $M = 0.9$. The combination of turbulence models and viscous models that provide the closest match to the experimental pressure coefficient distributions changes from low Reynolds numbers to very high Reynolds numbers. The ASM with *j-k* viscous modeling appeared to provide the best low Reynolds number comparison, while the ASM with only *k* thin-layer viscosity most closely matched the high Reynolds number static pressure coefficient distribution. There is likely a more applicable range of flow conditions for the advanced models, the resolution of which requires further advancement of the theories or implementation. The afterbody pressure drag variation observed between the experimental data and the computations with Reynolds number was small. The change with Reynolds number of the pressure coefficient distributions observed in the experimental data is qualitatively predicted by the CFD. This no-effect effect was discussed in cited high Reynolds numbers investigations. Most of the solutions using the nonlinear models predicted a separation point downstream of experimental flow visualization and parametric theory, except the SZL model.

## Appendix: Solution Nomenclature

An abbreviation designating the order of scheme, limiter, and viscous modeling is given in Table A1. All solutions were developed using the third-order accurate scheme for the convective terms, and second-order for the viscous diffusion terms. In Figs. 4, 6–10, 13, 14, 16–19, and 21, the scheme is denoted by the first number, i.e., 3, in the figure symbol table (Table A1). Only the min–mod limiter was utilized for this study and is denoted by the second number in the figure symbol table, i.e., 2. The viscous modeling was varied and is denoted by the third number.

**Table A1 Solution nomenclature**

| Abbreviation | Solution limiter | Viscous model |
|---|---|---|
| 311 | Van Albeda | *k* thin layer |
| 312 | Van Albeda | *j-k* coupled |
| 313 | Van Albeda | *j-k* uncoupled |
| 321 | min–mod | *k* thin layer |
| 322 | min–mod | *j-k* coupled |
| 323 | min–mod | *j-k* uncoupled |
| 331 | S–V | *k* thin layer |
| 332 | S–V | *j-k* coupled |
| 333 | S–V | *j-k* uncoupled |
| 341 | Modified S-V | *k* thin layer |
| 342 | Modified S-V | *j-k* coupled |
| 343 | Modified S-V | *j-k* uncoupled |

## References

[1] Reubush, D. E., and Putnam, L. E., "An Experimental and Analytical Investigation of the Effect on Isolated Boattail Drag of Varying Reynolds Number up to 130 $\times$ $10^6$," NASA TND-8210, May 1976.

[2] Reubush, D. E., "The Effect of Reynolds Number on Boattail Drag," AIAA Paper 75-63, Jan. 1975.

[3] Reubush, D. E., "The Effect of Reynolds Number on Boattail Drag of Two Wing-Body Configurations," AIAA Paper 75-1294, Sept. 1975.

[4] Reubush, D. E., "Experimental Investigation to Validate Use of Cryogenic Temperatures to Achieve High Reynolds Numbers in Boattail Pressure Testing," NASA TM X-3396, Aug. 1976.

[5] Carlson, J. R., "Application of Algebraic Reynolds Stress Turbulence Models Part 1: Incompressible Flat Plate," *Journal of Propulsion and Power*, Vol. 13, No. 5, 1997, pp. 610–619.

[6] Abdol-Hamid, K. S., Carlson, J. R., and Lakshmanan, B., "Application of Navier-Stokes Code PAB3D to Attached and Separated Flows for Use with $K$-$\varepsilon$ Turbulence Model," NASA TP-3480, Jan. 1994.

[7] Abdol-Hamid, K. S., "A Multiblock/Multizone Code (PAB3D-v2) for the Three-Dimensional Navier-Stokes Equations: Preliminary Applications," NASA CR-182032, Oct. 1990.

[8] Abdol-Hamid, K. S., Carlson, J. R., and Pao, S. P., "Calculation of Turbulent Flows Using Mesh Sequencing and Conservative Patch Algorithm," AIAA Paper 95-2336, July 1995.

[9] Abdol-Hamid, K. S.,"Implementation of Algebraic Stress Model in a General 3-D Navier-Stokes Method (PAB3D)," NASA CR-4702, Dec. 1995.

[10] Kilgore, R. A., Adcock, J. B., and Edward, J., "Flight Simulation Characteristics of the Langley High Reynolds Number Cryogenic Transonic Tunnel," AIAA Paper 74-80, Jan. 1974.

[11] Cahn, M. S., "An Experimental Investigation of Sting-Support Effects on Drag and a Comparison with Jet Effects at Transonic Speeds," NACA Rept. 1353, Jan. 1958.

[12] Abeyounis, W. K., "Boundary-Layer Separation on Isolated Boattail Nozzles," NASA TP-1226, Aug. 1978.